Spectral Energy Fluxes in Geostrophic Turbulence: Implications for Ocean Energetics

ROBERT B. SCOTT AND BRIAN K. ARBIC

Institute for Geophysics, Jackson School of Geosciences, The University of Texas at Austin, Austin, Texas

(Manuscript received 28 June 2005, in final form 12 July 2006)

ABSTRACT

The energy pathways in geostrophic turbulence are explored using a two-layer, flat-bottom, *f*-plane, quasigeostrophic model forced by an imposed, horizontally homogenous, baroclinically unstable mean flow and damped by bottom Ekman friction. A systematic presentation of the spectral energy fluxes, the mean flow forcing, and dissipation terms allows for a comprehensive understanding of the sources and sinks for baroclinic and barotropic energy as a function of length scale. The key new result is a robust inverse cascade of kinetic energy for both the baroclinic mode and the upper layer. This is consistent with recent observations of satellite altimeter data over the South Pacific Ocean. The well-known forward cascade of baroclinic potential and total energy was found to be very robust. Decomposing the spectral fluxes into contributions from different terms provided further insight. The inverse baroclinic kinetic energy cascade is driven mostly by an efficient interaction between the baroclinic velocity and the barotropic vorticity, the latter playing a crucial catalytic role. This cascade can be further enhanced by the baroclinic mode self-interaction, which is only present with nonuniform stratification (unequal layer depths). When model parameters are set such that modeled eddies compare favorably with observations, the inverse baroclinic kinetic energy cascade is actually much stronger than the well-known inverse cascade in the barotropic mode. The upper-layer kinetic energy cascade was found to dominate the lower-layer cascade over a wide range of parameters, suggesting that the surface cascade and time mean density stratification may be sufficient for estimating the depth-integrated cascade from ocean observations. This may find useful application in inferring the kinetic to gravitational potential energy conversion rate from satellite measurements.

1. Introduction

Two studies using satellite measurements of the sea surface have suggested an inverse kinetic energy (KE) cascade in the freely evolving upper ocean at scales larger than the first baroclinic mode deformation radius. In the first study, horizontal length scales of KE were observed to grow as mesoscale eddies traveled downstream of their formation region over the rough topography of the East Pacific Ridge (Stewart et al. 1996) in the Antarctic Circumpolar Current. A subtropical example is provided by the study of the North Pacific Subtropical Countercurrent and Hawaiian Lee Countercurrent, where eddy generation by baroclinic instability peaks in winter, followed by a period of apparently free evolution during which the eddy KE length scales were observed to grow (Kobashi and Kawamura 2002). Because the ocean is a rapidly rotating fluid the Taylor–Proudman theorem implies that its motion will be quasi-two-dimensional (Pedlosky 1987), and superficially one might conclude that the altimeter observations are consistent with the well-known inverse energy cascade of two-dimensional turbulence theory (Kraichnan and Montgomery 1980). However, for the stratified fluid the motion and corresponding theory is more complicated (Danilov and Gurarie 2000). The direction of the cascade can be different for the KE and potential energy (PE) and can be different depending upon the barotropic and baroclinic modes involved, as explained below.

For a stratified, rapidly rotating fluid the motions are still quasi-two-dimensional in the sense that horizontal velocity dominates the vertical velocity, however, the horizontal velocity varies with depth. In the quasigeostrophic (QG) context the vertical structure is conveniently handled with the orthogonal basis functions provided by the eigenfunctions of the Sturm–Liouville problem:

Corresponding author address: Robert B. Scott, Institute for Geophysics, Jackson School of Geosciences, The University of Texas at Austin, Pickle Research Campus, Bldg. 196, 10100 Burnet Rd., Austin, TX 78758.
E-mail: rscott@ig.utexas.edu

DOI: 10.1175/JPO3027.1

© 2007 American Meteorological Society

$$\frac{d}{dz}\left[\frac{f^2}{N^2(z)}\frac{d\phi}{dz}\right] = -\lambda^2\phi, \quad z \in (-H, 0),$$

where z is the vertical coordinate, H is the ocean depth, f is the Coriolis parameter, and $N(z)$ is the buoyancy frequency, given by $N^2 = -(g/\rho_0)d\sigma/dz$, where σ is potential density and ρ_0 is a reference density. The solutions are eigenfunctions called the "baroclinic modes," and the mth mode ϕ_m has m zero crossings. Thus the gravest mode, $m = 0$, called the barotropic mode, represents the depth-averaged flow, $\phi_0 =$ constant. The eigenvalues λ_m are the inverse of the deformation radii (dimension length) of the corresponding modes. At scales larger than the corresponding deformation radius geostrophic turbulence theory argues for a direct (i.e., downscale) cascade for the total baroclinic energy (Rhines 1977; Salmon 1980; Fu and Flierl 1980; Hua and Haidvogel 1986).

This is in the opposite sense to the barotropic KE cascade. Concurrent with the horizontal cascade, the geostrophic turbulence theory of Charney (1971) predicts a vertical transfer of energy from the baroclinic modes into the barotropic mode. For a fluid with strongly surface-intensified stratification, such as the ocean, the baroclinic modes interact inefficiently with the barotropic mode, and thus the slow vertical transfer provides a bottleneck to the horizontal cascade (Fu and Flierl 1980). Energy from higher baroclinic modes collects in the first mode and converges toward the deformation radius before it finally barotropizes (Smith and Vallis 2001). The inverse cascade is the final stage whereby energy in the barotropic mode near the deformation scale cascades toward larger scales.

Based on the geostrophic turbulence theory summarized above one might wonder if the inverse cascade observed at the oceanic surface represents the barotropic mode inverse cascade. But in fact the standard interpretation of the altimeter data is that it predominantly reflects the first baroclinic mode (Smith and Vallis 2001). The first baroclinic mode typically contains as much or more KE as the barotropic mode, with the higher modes representing the small residual. Also, the first baroclinic mode is more strongly weighted at the surface than the barotropic mode because of surface intensified, density stratification; Fig. 1 of Wunsch (1997) shows an example from the midlatitude North Atlantic; Eq. (11) of Arbic and Flierl (2004, hereinafter AF) illustrates the point for a two-layer model. The presumed dominance of the first baroclinic mode is consistent with the observed altimeter signals, which in the midlatitudes reveal Rossby waves and eddies propagating westward at the speeds corresponding to first baroclinic motions (B. Qiu 2005, personal communication) modified by the background potential vorticity gradients (Killworth et al. 1997).

The inverse KE cascade seen in the altimeter data was recently studied further by Scott and Wang (2005, hereinafter SW).[1] They diagnosed the spectral KE flux Π_K from the satellite altimeter data to directly determine the direction of the cascade near the surface. The spectral flux Π_K is defined as the rate of transfer of KE from scales with wavelength $\lambda > 2\pi/K$ to scales with wavelength $\lambda < 2\pi/K$, where K is the total horizontal wavenumber. Throughout the South Pacific Ocean, Π_K had a universal shape that revealed a source of KE from a range of length scales near and larger than the deformation scale, with about ¾ (¼) of the energy cascading to larger (smaller) scales. Thus there was a net inverse cascade and a clear upscale flux at scales larger than the deformation scale. Since the altimeter measures only the surface geostrophic flow, little could be definitively said about the vertical structure of the diagnosed cascade. Important questions remain: 1) Is the inverse KE cascade seen at the oceanic surface due to the barotropic mode? 2) Or is it possible that the baroclinic KE experiences an inverse cascade? 3) How are the cascades of the surface and baroclinic modes related? 4) Given knowledge of the surface spectral flux, what additional information is needed to infer the depth-integrated spectral flux?

These questions are addressed here. Questions 1 and 2 may be important for assessing the relevance of scaling theories of turbulent eddies to the real ocean since to date these theories (Larichev and Held 1995; Held and Larichev 1996; Spall 2000; Smith and Vallis 2002) do not take into account an upscale cascade of baroclinic KE near the deformation scale. Addressing question 3 will help to connect altimeter measurements and geostrophic turbulence theory.

Although the main focus of this study is the direction of the baroclinic cascade, question 4 above deserves some emphasis for its practical importance. Knowledge of the depth-integrated spectral KE flux would allow one to estimate the conversion rate of gravitational potential energy to KE, an important unknown in the mechanical energy cycles of the World Ocean. Previous estimates based upon observations have been very crude, invoking the GM mixing scheme with uncertain parameters (Wunsch and Ferrari 2004). Altimeter data provide direct estimates of spectral flux only near the

[1] Established theory is agnostic about the KE component of the baroclinic cascade. While the discussion section of SW is more clear about this, the abstract of SW overstates the discrepancy with observations. Author Scott thanks S. Danilov for bringing this to his attention.

TABLE 1. Definitions and properties; "bt," "bc," and "C" denote barotropic, baroclinic, and conservative.

Term	Definition	Simplified	C	Line
bc eqn				
$N_{\mathrm{bc,bt,bc}}$	$\langle\psi^{>}_{\mathrm{bc},K}\mathbf{J}(\psi_{\mathrm{bt}}, q_{\mathrm{bc}})\rangle$	$C_K + \Pi^{\mathrm{pe}}_{\mathrm{bc},K}$	No	
C_K	$\langle\psi^{>}_{\mathrm{bc},K}\mathbf{J}(\psi_{\mathrm{bt}}, \nabla^2\psi_{\mathrm{bc}})\rangle$	Does not simplify	No	Maroon
$\Pi^{\mathrm{pe}}_{\mathrm{bc},K}$	$\langle\psi^{>}_{\mathrm{bc},K}\mathbf{J}(\psi_{\mathrm{bt}}, -\psi_{\mathrm{bc}}/L_D^2)\rangle$	$\langle\psi_{\mathrm{bt}}\mathbf{J}(\psi^{>}_{\mathrm{bc},K}, \psi^{<}_{\mathrm{bc},K}/L_D^2)\rangle$	Yes	Purple
$N_{\mathrm{bc,bc,bt}}$	$\langle\psi^{>}_{\mathrm{bc},K}\mathbf{J}(\psi_{\mathrm{bc}}, q_{\mathrm{bt}})\rangle$	$\langle\psi^{>}_{\mathrm{bc},K}\mathbf{J}(\psi^{<}_{\mathrm{bc},K}, \nabla^2\psi_{\mathrm{bt}})\rangle$	Yes	
$N_{\mathrm{bc,bc,bc}}$	$\langle\psi^{>}_{\mathrm{bc},K}\epsilon\mathbf{J}(\psi_{\mathrm{bc}}, q_{\mathrm{bc}})\rangle$	$\epsilon\langle\psi^{>}_{\mathrm{bc},K}\mathbf{J}(\psi^{<}_{\mathrm{bc},K}, \nabla^2\psi_{\mathrm{bc}})\rangle$	Yes	
$\Pi^{\mathrm{ke}}_{\mathrm{bc},K}$	$N_{\mathrm{bc,bc,bt}} + N_{\mathrm{bc,bc,bc}}$	Does not simplify	Yes	Black
$F_{\mathrm{bc,bc,bc}}$	$\langle\psi^{>}_{\mathrm{bc},K}\overline{u}_{\mathrm{bc}}(\partial/\partial x)(\epsilon\nabla^2\psi_{\mathrm{bc}})\rangle$	0		
$F_{\mathrm{bc,bc,bt}}$	$\langle\psi^{>}_{\mathrm{bc},K}\overline{u}_{\mathrm{bc}}(\partial/\partial x)(q_{\mathrm{bt}} + \psi_{\mathrm{bt}}/L_D^2)\rangle$	$\langle\psi^{>}_{\mathrm{bc},K}\overline{u}_{\mathrm{bc}}(\partial/\partial x)(\nabla^2\psi^{>}_{\mathrm{bt},K} + \psi^{>}_{\mathrm{bt},K}/L_D^2)\rangle$	No	Green
$F_{\mathrm{bc,bt,bc}}$	$\langle\psi^{>}_{\mathrm{bc},K}\overline{u}_{\mathrm{bt}}(\partial/\partial x)q_{\mathrm{bc}}\rangle$	0		
$D_{\mathrm{bc,bt,bc}}$	$\langle\psi^{>}_{\mathrm{bc},K}R_{\mathrm{bt}}[\delta/(1+\delta)\nabla^2\psi_{\mathrm{bc}}]\rangle$	$-2R_{\mathrm{bt}}[\delta/(1+\delta)]\mathrm{KE}_{\mathrm{bc},K}$	No	
$D_{\mathrm{bc,bt,bt}}$	$-\langle\psi^{>}_{\mathrm{bc},K}R_{\mathrm{bt}}[\sqrt{\delta}/(1+\delta)]\nabla^2\psi_{\mathrm{bt}}\rangle$	$-\langle\psi^{>}_{\mathrm{bc},K}R_{\mathrm{bt}}[\sqrt{\delta}/(1+\delta)]\nabla^2\psi^{>}_{\mathrm{bt},K}\rangle$	No	
	$D_{\mathrm{bc,bt,bt}} + D_{\mathrm{bc,bt,bc}}$	Does not simplify	No	Red
Σ_{bc}	$\Sigma_{q,r}(N_{\mathrm{bc},q,r} + F_{\mathrm{bc},q,r} + D_{\mathrm{bc},q,r})$	0	Yes	Cyan
bt eqn				
$N_{\mathrm{bt,bt,bt}}$	$\langle\psi^{>}_{\mathrm{bt},K}\mathbf{J}(\psi_{\mathrm{bt}}, q_{\mathrm{bt}})\rangle$	$\langle\psi^{>}_{\mathrm{bt},K}\mathbf{J}(\psi^{<}_{\mathrm{bt},K}, \nabla^2\psi_{\mathrm{bt}})\rangle$	Yes	Black
$N_{\mathrm{bt,bc,bc}}$	$\langle\psi^{>}_{\mathrm{bt},K}\mathbf{J}(\psi_{\mathrm{bc}}, q_{\mathrm{bc}})\rangle$	Does not simplify	No	Maroon
$F_{\mathrm{bt,bc,bc}}$	$\langle\psi^{>}_{\mathrm{bt},K}\overline{u}_{\mathrm{bc}}(\partial/\partial x)\nabla^2\psi_{\mathrm{bc}}\rangle$	$\langle\psi^{>}_{\mathrm{bt},K}\overline{u}_{\mathrm{bc}}(\partial/\partial x)\nabla^2\psi^{>}_{\mathrm{bc},K}\rangle$	No	Green
$F_{\mathrm{bt,bt,bt}}$	$\langle\psi^{>}_{\mathrm{bt},K}\overline{u}_{\mathrm{bt}}(\partial/\partial x)\nabla^2\psi_{\mathrm{bt}}\rangle$	0		
$D_{\mathrm{bt,bt,bt}}$	$\langle\psi^{>}_{\mathrm{bt},K}R_{\mathrm{bt}}[q_{\mathrm{bt}}/(1+\delta)]\rangle$	$-2R_{\mathrm{bt}}[1/(1+\delta)]\mathrm{KE}_{\mathrm{bt},K}$	No	
$D_{\mathrm{bt,bt,bc}}$	$-\langle\psi^{>}_{\mathrm{bt},K}R_{\mathrm{bt}}[\sqrt{\delta}/(1+\delta)]\nabla^2\psi_{\mathrm{bc}}\rangle$	$D_{\mathrm{bc,bt,bt}}$	No	
	$D_{\mathrm{bt,bt,bt}} + D_{\mathrm{bt,bt,bc}}$	Does not simplify	No	Red
Σ_{bt}	$\Sigma_{q,r}(N_{\mathrm{bt},q,r} + F_{\mathrm{bt},q,r} + D_{\mathrm{bt},q,r})$	0	Yes	Cyan

surface. However, we will show through analysis of an idealized model that the depth-integrated spectral flux is completely dominated by the upper-layer flux for most parameter settings, suggesting that surface information combined with climatological density data may be sufficient to infer the depth-integrated flux.

These questions are addressed using a simple numerical model of geostrophic turbulence: a two-layer, QG model on a flat-bottom f plane, driven by an imposed, baroclinically unstable, mean flow and damped by bottom friction, described in section 3. The model has been run with a wide range of parameters, spanning regimes with eddies that compare well with observations and those that differ significantly from observations. Diagnosing the spectral fluxes revealed the energy cascades, which we describe in the context of the complete length scale-dependent mechanical energy budget, derived in section 2. We also computed the spectral energy density budget, which is obtained from the convergence of the aforementioned budget. We call the latter the "local budget" since it contains sources and sinks at a particular wavenumber. The former budget will be called the "integral budget" since its terms are the integral of the local budget over a semi-infinite subset of the wavenumber axis. The advantage for our purposes is that the cascade directions are immediately apparent in the integral but not the local budget. The answers to questions 1 and 2 are described in section 4, and questions 3 and 4 are addressed in section 5. We summarize our findings in the conclusions (section 6).

2. Theory

Below in section 2a we derive the equations of the mechanical energy budget for the baroclinic and barotropic modes as a function of length scale. We therein define the spectral energy fluxes, forcing and dissipation terms for flow smaller than the length scale in question. These form the main diagnostics used here and will be referred to collectively as "integral budget sources." From the integral budget we derive the spectral density budget (via convergence), the terms of which we refer to as "local sources." This is the opposite order to the typical development in which the integral budget terms are obtained by integrating the local sources from some wavenumber to infinity (Larichev and Held 1995). However, many of the properties of interest are immediately apparent from the formulation presented here. Also, an implicit angular average avoids the typical assumption of isotropy used to define the spectral density in terms of total horizontal wavenumber K, as in, for example, Lesieur (1997). To aid in keeping track of the plethora of terms in the budgets, we introduce a succinct notation from which it is immediately apparent which terms in the governing equations led to the corresponding energy budget term. All terms and their properties are summarized in Tables 1 and 2.

In section 2b we provide a physical interpretation of terms in the baroclinic integral budget (with obvious extensions applying to the barotropic budget). In section 2c we show how to transform from the integral and local budgets. In section 2d we derive the corresponding terms for each layer separately.

a. The modal, scale-dependent, integral mechanical energy budget

We apply the method of Frisch (1995, his section 2.4) to the two-layer, potential vorticity (PV) equations in modal form:

$$\frac{\partial q_{\rm bc}}{\partial t} = -\mathbf{J}(\psi_{\rm bt}, q_{\rm bc}) - \mathbf{J}(\psi_{\rm bc}, q_{\rm bt}) - \epsilon\mathbf{J}(\psi_{\rm bc}, q_{\rm bc}) - \overline{u}_{\rm bc}\frac{\partial}{\partial x}\left(\epsilon\nabla^2\psi_{\rm bc} + q_{\rm bt} + \frac{\psi_{\rm bt}}{L_D^2}\right) - \overline{u}_{\rm bt}\frac{\partial}{\partial x}q_{\rm bc} - R_{\rm bt}\left(\frac{\delta}{1+\delta}\nabla^2\psi_{\rm bc} - \frac{\sqrt{\delta}}{1+\delta}\nabla^2\psi_{\rm bt}\right) \quad \text{and}$$

$$\frac{\partial q_{\rm bt}}{\partial t} = -\mathbf{J}(\psi_{\rm bt}, q_{\rm bt}) - \mathbf{J}(\psi_{\rm bc}, q_{\rm bc}) - \overline{u}_{\rm bc}\frac{\partial}{\partial x}\nabla^2\psi_{\rm bc} - \overline{u}_{\rm bt}\frac{\partial}{\partial x}q_{\rm bt} - R_{\rm bt}\left(\frac{q_{\rm bt}}{1+\delta} - \frac{\sqrt{\delta}}{1+\delta}\nabla^2\psi_{\rm bc}\right), \quad (1)$$

where subscripts bt and bc refer to the barotropic and baroclinic modes, $R_{\rm bt}$ is just the bottom friction parameter,[2] L_D is the deformation radius, and $\epsilon = (1 - \delta)/\sqrt{\delta}$. The stratification parameter $\delta = H_1/H_2$, where H is layer depth and subscripts 1 and 2 refer to upper and lower layer, respectively. The imposed zonal mean flows are $\overline{u}_{\rm bc}$ and $\overline{u}_{\rm bt}$. The streamfunctions, potential vorticities, and KE are defined as in AF:

$$\psi_{\rm bt} = \frac{\delta\psi_1 + \psi_2}{1+\delta},$$

$$\psi_{\rm bc} = \frac{\sqrt{\delta}(\psi_1 - \psi_2)}{1+\delta},$$

$$q_{\rm bt} = \nabla^2\psi_{\rm bt},$$

$$q_{\rm bc} = \nabla^2\psi_{\rm bc} - \frac{1}{L_D^2}\psi_{\rm bc},$$

$$\mathrm{KE}_{\rm bt} = \frac{1}{2}\int_0^{L_y}\int_0^{L_x}(\nabla\psi_{\rm bt})^2\,dx\,dy, \quad \text{and}$$

$$\mathrm{KE}_{\rm bc} = \frac{1}{2}\int_0^{L_y}\int_0^{L_x}(\nabla\psi_{\rm bc})^2\,dx\,dy, \quad (2)$$

[2] It is arbitrarily identified with the barotropic mode for notational convenience later.

TABLE 2. Physical meaning of terms and names; "BF" denotes bottom friction.

Term	Meaning	Name
bc eqn		
$N_{\rm bc,bt,bc}$	bt stirring	bt stirring
C_K	$\mathrm{KE}_{\rm bc} \rightarrow \mathrm{KE}_{\rm bt}$	Barotropization
$\Pi^{\rm pe}_{{\rm bc},K}$	Flux $\mathrm{PE}_{\rm bc}$	PE flux
$N_{\rm bc,bc,bt}$	Partial flux $\mathrm{KE}_{\rm bc}$	Catalytic flux
$N_{\rm bc,bc,bc}$	Partial flux $\mathrm{KE}_{\rm bc}$	bc self-interaction
$\Pi^{\rm ke}_{{\rm bc},K}$	Total flux $\mathrm{KE}_{\rm bc}$	bc KE flux
$F_{\rm bc,bc,bc}$	Mean shear bc interaction	—
$F_{\rm bc,bc,bt}$	Mean shear bt interaction	Mean shear forcing
$F_{\rm bc,bt,bc}$	Mean bt flow forcing	—
$D_{\rm bc,bt,bc}$	BF dissipation of bc energy	BF dissipation
$D_{\rm bc,bt,bt}$	BF scattering KE into bc mode	Scattering
$D_{\rm bc,bt,bt} + D_{\rm bc,bt,bc}$	Net BF dissipation of bc energy	Net bc dissipation
$\Sigma_{\rm bc}$	Net sources or bc tendency	Residual
bt eqn		
$N_{\rm bt,bt,bt}$	Flux $\mathrm{KE}_{\rm bt}$	bt self-interaction
$N_{\rm bt,bc,bc}$	$\mathrm{KE}_{\rm bt} \rightarrow \mathrm{KE}_{\rm bc}$	Barotropization
$F_{\rm bt,bc,bc}$	Mean shear bc interaction	bt forcing
$F_{\rm bt,bt,bt}$	Mean bt flow forcing	NA
$D_{\rm bt,bt,bt}$	BF dissipation of bt energy	bt dissipation
$D_{\rm bt,bt,bt}$	BF scattering KE into bc mode	Scattering
$D_{\rm bt,bt,bt} + D_{\rm bt,bt,bc}$	Net BF dissipation of bt energy	Net bt dissipation
$\Sigma_{\rm bt}$	Net sources or bt tendency	Residual

where L_x and L_y are the horizontal dimensions of the domain.

To find the integral budget as a function of length scale we need to define a high-pass filter. For solutions of Eq. (1) on an enclosed or periodic domain, it is convenient to represent the solution $\psi(x, y, t)$ in terms of a Fourier series,

$$\psi(x, y, t) = \sum_{k,l}\hat{\psi}_{k,l}(t)e^{i(kx+ly)}. \quad (3)$$

The horizontal wavenumber vector is $(k, l) = 2\pi(m/L_x, n/L_y)$, where $m, n \in Z$, and the sum is over all wavenumbers. Then we can define the high-pass filter with cutoff total wavenumber K as a simple truncation,

$$\psi^{>}_K(x, y, t) = \sum_{k^2+l^2>K^2}\hat{\psi}_{k,l}(t)e^{i(kx+ly)}, \quad (4)$$

with an obvious extension to a low-pass filter $\psi^{<}_K = \psi - \psi^{>}_K$. Projecting the PV Eqs. (1) onto $-\psi^{>}_{{\rm bc},K}$ and $-\psi^{>}_{{\rm bt},K}$ one obtains the mechanical energy budget for the baroclinic and barotropic small-scale flow (the integral budget). The former has two components,

$$\left\langle -\psi^{>}_{{\rm bc},K}\frac{\partial q_{\rm bc}}{\partial t}\right\rangle = \frac{1}{2}\frac{\partial}{\partial t}\left\langle(\nabla\psi^{>}_{{\rm bc},K})^2 + \frac{(\psi^{>}_{{\rm bc},K})^2}{L_D^2}\right\rangle, \quad (5)$$

where $\langle\rangle$ denotes average over the domain. The terms on the right of Eq. (5) are easily identified as the kinetic energy $\mathrm{KE}^{>}_{\mathrm{bc},K}$ and potential energy $\mathrm{PE}^{>}_{\mathrm{bc},K}$ *of the flow with horizontal scales smaller than* $2\pi/K$. This is the key fact used to interpret the remaining terms in the integral budget. We use E to denote total energy $E = \mathrm{KE} + \mathrm{PE}$. Because of the rigid lid approximation leading to the governing Eqs. (1), the potential energy of barotropic flow is zero and

$$\left\langle -\psi^{>}_{\mathrm{bt},K}\frac{\partial q_{bt}}{\partial t}\right\rangle = \frac{1}{2}\frac{\partial}{\partial t}\langle\nabla\psi^{>}_{\mathrm{bt},K}\rangle^2 \equiv \frac{\partial E^{>}_{\mathrm{bt},K}}{\partial t}. \qquad (6)$$

In a statistically steady state the tendency terms vanish as a balance is reached between the remaining terms. Our goal in this section is to define and interpret each term. In section 4 we present each term in equilibrated numerical simulations of the governing Eqs. (1). An alternative derivation that may be more familiar to some readers is obtained from the energy spectral density equation. The energy spectral density is obtained multiplying the Fourier transform of the governing Eqs. (1) by $-\hat{\psi}^*$, integrating over all directions and taking the expected value. For instance, for the baroclinic equation,

$$\left\langle -\hat{\psi}^*_{\mathrm{bc}}\frac{\partial\hat{q}_{\mathrm{bc}}}{\partial t}\right\rangle = \frac{\partial E_{\mathrm{bc}}(K)}{\partial t}.$$

The integral energy budget is related to the spectral density by the semi-infinite integral,

$$E^{>}_{\mathrm{bc},K} = \int_K^\infty E_{\mathrm{bc}}(K).$$

In fact this is how we calculated all the quantities derived below because it turned out to be more efficient computationally, and gave equivalent results within round-off error.

The terms on the rhs of Eq. (1) have been grouped into three lines: nonlinear advection, forcing by the mean flow, and dissipation by bottom friction. Projected onto $-\psi^{>}_{\mathrm{bc},K}$ and $-\psi^{>}_{\mathrm{bt},K}$, these will be identified, respectively, as $N_{p,q,r}(K)$, $F_{p,q,r}(K)$, and $D_{p,q,r}(K)$, where subscript p identifies the mode of $\psi^{>}_K$, q the first, and r the second factor on the rhs of Eq. (1), respectively. The explicit K dependence will be dropped for notational convenience. The barotropic (baroclinic) mode is indicated with bt (bc). Thus, for example, $N_{\mathrm{bc,bt,bc}} = \langle\psi^{>}_{\mathrm{bc},K}J(\psi_{\mathrm{bt}}, q_{\mathrm{bc}})\rangle$ and $D_{\mathrm{bt,bt,bc}} = \langle-\psi^{>}_{\mathrm{bt},K}R_{\mathrm{bt}}[\sqrt{\delta}/(1+\delta)]\nabla^2\psi_{\mathrm{bc}}\rangle$. Formally the scale-dependent integral energy budget is written

$$\frac{\partial E^{>}_{p,K}}{\partial t} = \sum_{q,r}(N_{p,q,r} + F_{p,q,r} + D_{p,q,r}), \qquad (7)$$

where nonexistent terms are assumed to be zero, for example, $N_{\mathrm{bt,bc,bt}} = 0$.

In section 2b we interpret all terms for the baroclinic integral budget. The interpretation for the corresponding barotropic integral budget is straightforward. A key concept is whether or not a term is "conservative" *within a given mode*. For instance, $N_{\mathrm{bc,bt,bc}}$, the well-known "barotropic stirring of baroclinic PV," is not conservative within the baroclinic mode because it transfers energy to the barotropic mode. Care must be taken not to interpret this and other nonconservative terms as redistributing energy between different horizontal wavenumbers, a point that we suspect might not be well appreciated. For instance, Hua and Haidvogel (1986, their Fig. 11) conclude that because the total spectral transfer is negative at large scale ($L \sim 2L_D$) for each baroclinic mode $m = 1, 2, 3$, there must be a forward cascade of baroclinic energy, where their T_{klm} corresponds to

$$T_{\mathrm{klm}}(K) = \sum_{q,r} -\frac{\partial N_{m,q,r}}{\partial K}, \quad K^2 = k^2 + l^2,$$

for a given mode m. In particular, we suggest the negative T_{klm} at large scale is at least partly due to barotropization, which we found to be significant at scales $L \sim 2L_D$. Thus we avoid the term "flux" for such nonconservative source terms.[3] Hence, as done by Larichev and Held (1995), we separate out the vortex stretching part of this term, which *is* conservative.

The reader may wish to turn now to Tables 1 and 2 and refer to section 2b only for clarification. The colors listed in Table 1 are used consistently and the runs are described in Table 3, and therefore one should be able to interpret all figures based only upon the tables.

b. Interpretation of baroclinic sources and sinks

The $N_{\mathrm{bc,bt,bc}}$ term has received much consideration since the "barotropic stirring" is traditionally argued to strain q_{bc}, and thereby drive a forward baroclinic total energy cascade (Salmon 1980; Hua and Haidvogel 1986). It can be divided into two contributions:

$$\langle\psi^{>}_{\mathrm{bc},K}\mathbf{J}(\psi_{\mathrm{bt}}, q_{\mathrm{bc}})\rangle \equiv N_{\mathrm{bc,bt,bc}} = C_K + \Pi^{\mathrm{pe}}_{\mathrm{bc},K}. \qquad (8)$$

The term

$$C_K \equiv \langle\psi^{>}_{\mathrm{bc},K}\mathbf{J}(\psi_{\mathrm{bt}}, \nabla^2\psi_{\mathrm{bc}})\rangle \qquad (9)$$

[3] Of course it is conservative for the total energy, since it "fluxes" energy between different modes. Also note that the energy and enstrophy properties are different, for example, barotropic stirring exchanges energy between modes, but not enstrophy.

TABLE 3. Summary of run simulation parameters and their resulting statistics. $\delta = H_1/H_2$, i.e., ratio of layer depths, TP is the throughput parameter, $(u_1 - u_2)/L_D R_2$, $B \equiv \mathrm{KE_{bc}}/\mathrm{KE_{bt}}$, $S \equiv \langle(\nabla\psi_1)^2\rangle/\langle(\nabla\psi_2)^2\rangle$, and K_{bc} and K_{bt} are the centroids of the baroclinic and barotropic kinetic energy spectra, in units of $L_D^{-1}\epsilon = (1 - \delta)/\sqrt{\delta}$.

Run No.	δ	TP	Friction	B	S	K_{bc}	K_{ht}	ϵ	Snapshots
1	0.2	2.5	Moderate	1.5	32	0.90	0.79	1.79	167
2	0.2	10	Weak	0.35	6.3	0.90	0.53	1.79	92
3	1	1.0	Moderate	0.66	11	0.90	0.85	0	10
4	1	10	Weak	0.047	1.2	0.93	0.35	0	78

arises from barotropic flow stirring baroclinic relative vorticity and is not simply a redistribution of baroclinic energy between different horizontal scales because $C_{K=0} \neq 0$. In fact, in the limit $K = 0$ we will find that a corresponding term arises in the barotropic equation with a minus sign, and thus it represents "barotropization," that is, a conversion of baroclinic energy into barotropic energy. In fact C_K represents a loss of $\mathrm{KE}^{>}_{\mathrm{bc},K}$ as opposed to PE since there is no L_D involved. This can be proven rigorously (G. Flierl 2006, personal communication) using the KE equation, which one derives from the relative vorticity equation, as in SW.

The second contribution

$$\Pi^{\mathrm{pe}}_{\mathrm{bc},K} \equiv \left\langle \psi^{>}_{\mathrm{bc},K}\mathbf{J}\left(\psi_{\mathrm{bt}}, \frac{-\psi_{\mathrm{bc}}}{L_D^2}\right)\right\rangle = \left\langle \psi_{\mathrm{bt}}\mathbf{J}\left(\psi^{>}_{\mathrm{bc},K}, \frac{\psi^{<}_{\mathrm{bc},K}}{L_D^2}\right)\right\rangle \tag{10}$$

is correctly identified as a spectral energy flux, since it redistributes energy between different horizontal length scales. (Here and in the following we have used simple properties of the Jacobian, which are provided in the appendix.) This is clear since $\Pi^{\mathrm{pe}}_{\mathrm{bc},K=0} = 0$, which follows because obviously $\psi^{<}_{\mathrm{bc},K=0} = 0$. This a PE flux, which is apparent from the factor of $1/L_D^2$. Curiously, the rhs of Eq. (10) reveals that only the small-scale flow ($\psi^{>}_{\mathrm{bc},K}$) advecting the large-scale flow ($\psi^{<}_{\mathrm{bc},K}/L_D^2$) contributes. The term $\Pi^{pe}_{bc,K}$ arises from triads denoted "UEE" by Salmon (1980), for which the exchange of energy with the barotropic mode becomes small, except when the barotropic wavenumber approaches $1/L_D$ (Salmon 1978, 1980). But this approximation is not to be confused with our exact statement here that $\Pi^{\mathrm{pe}}_{\mathrm{bc},K}$ does not exchange energy with the barotropic mode. The negligible exchanges must cancel exactly.

The next two terms in Table 1 are both fluxes. The first,

$$N_{\mathrm{bc,bc,bt}} \equiv \langle \psi^{>}_{\mathrm{bc},K}\mathbf{J}(\psi_{\mathrm{bc}}, q_{\mathrm{bt}})\rangle = \langle \psi^{>}_{\mathrm{bc},K}\mathbf{J}(\psi^{<}_{\mathrm{bc},K}, \nabla^2\psi_{\mathrm{bt}})\rangle, \tag{11}$$

involves the barotropic mode and yet conserves energy within the baroclinic mode. Thus the barotropic mode is playing a catalytic role, so we will call this the "catalytic (baroclinic KE) flux." The second,

$$N_{\mathrm{bc,bc,bc}} \equiv \langle \psi^{>}_{\mathrm{bc},K}\epsilon J(\psi_{\mathrm{bc}}, q_{\mathrm{bc}})\rangle = \epsilon\langle \psi^{>}_{\mathrm{bc},K}\mathbf{J}(\psi^{<}_{\mathrm{bc},K}, \nabla^2\psi_{\mathrm{bc}})\rangle, \tag{12}$$

involves only the baroclinic mode and hence we will call it the "baroclinic self-interaction." The self-interaction results from triads not considered by Salmon (1978, 1980) because $\epsilon = 0$ for $\delta = 1$ (Flierl 1978). Together, these form the baroclinic KE flux,

$$\Pi^{\mathrm{ke}}_{\mathrm{bc},K} \equiv N_{\mathrm{bc,bc,bc}} + N_{\mathrm{bc,bc,bt}}.$$

Using this formulation it is immediately clear, using integration by parts, that the first forcing term does no work:

$$F_{\mathrm{bc,bc,bc}} \equiv \left\langle \psi^{>}_{\mathrm{bc},K}\overline{u}_{\mathrm{bc}}\frac{\partial}{\partial x}(\epsilon\nabla^2\psi_{\mathrm{bc}})\right\rangle = 0, \quad \forall K.$$

Similarly, the mean barotropic flow does no work since

$$F_{\mathrm{bc,bt,bc}} \equiv \left\langle \psi^{>}_{\mathrm{bc},K}\overline{u}_{\mathrm{bt}}\frac{\partial}{\partial x}q_{\mathrm{bc}}\right\rangle = 0, \quad \forall K.$$

However the interaction of the mean shear with the baroclinic flow does force the baroclinic energy. Thus the "mean shear forcing" is

$$F_{\mathrm{bc,bc,bt}} \equiv \left\langle \psi^{>}_{\mathrm{bc},K}\overline{u}_{\mathrm{bc}}\frac{\partial}{\partial x}\left(q_{\mathrm{bt}} + \frac{\psi_{\mathrm{bt}}}{L_D^2}\right)\right\rangle = \left\langle \overline{u}_{\mathrm{bc}}\psi^{>}_{\mathrm{bc},K}\frac{\partial}{\partial x}\left(\nabla^2\psi^{>}_{\mathrm{bt},K} + \frac{\psi^{>}_{\mathrm{bt},K}}{L_D^2}\right)\right\rangle.$$

The dissipation term has two contributions. One is a sign-definite "baroclinic dissipation" of energy:

$$D_{\mathrm{bc,bt,bc}} \equiv \left\langle \psi^{>}_{\mathrm{bc},K}R_{\mathrm{bt}}\left(\frac{\delta}{1+\delta}\nabla^2\psi_{\mathrm{bc}}\right)\right\rangle = -2R_{\mathrm{bt}}\left(\frac{\delta}{1+\delta}\right)\mathrm{KE}^{>}_{\mathrm{bc},K}.$$

Interestingly the bottom friction cross term is sign indefinite and indeed was actually found to scatter energy into the baroclinic mode, much as Treguier and Hua (1988) found for the bottom topography. This "scattering" term is represented by

$$D_{\mathrm{bc,bt,bt}} \equiv -\left\langle \psi^{>}_{\mathrm{bc},K} R_{\mathrm{bt}} \frac{\sqrt{\delta}}{1+\delta} \nabla^2 \psi_{\mathrm{bt}} \right\rangle.$$

A similar development allows one to derive and interpret all the terms in the integral, scale-dependent, barotropic energy equation. The results are summarized in Tables 1 and 2.

c. Spectral energy density

Taking the convergence of $E^{>}_{\mathrm{bc},K}$ or $E^{>}_{\mathrm{bt},K}$, one obtains the corresponding spectral energy density:

$$E(K) \equiv -\frac{\partial E^{>}_{K}}{\partial K}. \tag{13}$$

Thus the convergence of Eq. (7) gives the spectral density budget terms. The nonlinear terms give rise to the spectral transfer[4] terms, commonly denoted as $T(K)$,

$$-\frac{\partial N^{>}_{K}}{\partial K} = T(K).$$

No assumption of isotropy was made. The formulation in section 2a implicitly involves an integral over all directions of the wavenumber vector.

d. Layer scale-dependent integral mechanical energy budgets

To make the connection with the altimeter observations, which correspond most directly to the model's upper layer, we will need the layer form of Eq. (7). This is derived in the same way, but starting from the layer form of Eq. (1) [see, e.g., Arbic and Flierl 2003, their Eqs. (17) and (18)]. In particular, one projects the layer PV equations onto $-\psi^{>}_{i,K} H_i/(H_1 + H_2)$. The result is

$$\frac{\partial \mathrm{KE}^{>}_{i,K} + \mathrm{PE}^{>}_{i,K}}{\partial t} = N_{i,K} + F_{i,K} + D_{i,K} + C_{i,K} = 0, \tag{14}$$

where $i \in \{1, 2\}$ refers to upper or lower layer, respectively, and the second equality assumes a statistically steady state. The lhs is the evolution of the total energy in each layer. The terms on the rhs are as follows:

$$\begin{aligned} N_{i,K} &= \left(\frac{H_i}{H_1 + H_2}\right) \langle \psi^{>}_{i,K} \mathbf{J}(\psi_i, q_i) \rangle \\ &= \left(\frac{H_i}{H_1 + H_2}\right) \langle \psi^{>}_{i,K} \mathbf{J}(\psi^{<}_{i,K}, \nabla^2 \psi_i) \rangle \\ &\quad - \gamma \langle \psi^{>}_{i,K} \mathbf{J}(\psi^{<}_{i,K}, \psi_{3-i}) \rangle \end{aligned} \tag{15}$$

where $\gamma = \delta/(1 + \delta)^2 L_D^2$. The first term on the rhs is a KE flux and the second is a PE flux,

$$N_{i,K} = \Pi^{\mathrm{ke}}_{i,K} + \Pi^{\mathrm{pe}}_{i,K}.$$

The real ocean analog of $\langle \psi^{>}_{1,K} J(\psi^{<}_{1,K}, \nabla^2 \psi_1) \rangle$ is observable with satellite measurements. By combining this with an estimate of layer depths one can infer $\Pi^{\mathrm{ke}}_{1,K}$, and, as we will see in section 5, much can be inferred from $\Pi^{\mathrm{ke}}_{1,K}$.

The forcing terms, which represent driving by the large-scale mean flow maintained by wind and buoyancy in the real ocean, are given by

$$F_{i,K} = \left(\frac{H_i}{H_1 + H_2}\right) \left\langle \psi^{>}_{i,K} \overline{u}_i \frac{\partial q_i}{\partial x} \right\rangle = \gamma \overline{u}_i \left\langle \psi^{>}_{i,K} \frac{\partial \psi^{>}_{3-i,K}}{\partial x} \right\rangle. \tag{16}$$

Here $\overline{u}_2 = 0$ so $F_{2,K} = 0$, $\forall K$. The term that exchanges energy between layers is

$$C_{i,K} = \left\langle \psi^{>}_{i,K} \gamma \frac{\partial \psi^{>}_{3-i,K}}{\partial t} \right\rangle = -C_{3-i,K}, \tag{17}$$

where the second equality arises in the statistically steady state, whereby

$$\frac{\partial \langle \psi^{>}_{1,K} \psi^{>}_{2,K} \rangle}{\partial t} = 0.$$

The dissipation term arises only in the lower layer,

$$D^{>}_{2,K} = \left(\frac{H_2}{H_1 + H_2}\right) \langle \psi^{>}_{2,K} R_2 \nabla^2 \psi_2 \rangle = -2 R_2 \mathrm{KE}^{>}_{2,K},$$

with $R_2 = R_{\mathrm{bt}}$.

3. Model

The model runs analyzed here are a subset of those analyzed earlier by AF. They are *f*-plane simulations of a doubly periodic, flat-bottom, two-layer QG model forced by an imposed, horizontally homogenous, vertically sheared (baroclinically unstable) mean flow and damped by bottom Ekman friction; see Arbic and Flierl (2003) or AF for a description of the model. Our model is simple but allows us to look for an inverse baroclinic KE cascade. The model equations are the layer versions of Eq. (1) but with small-scale dissipation in the

[4] Unfortunately, the terminology is not fixed. For instance, Salmon (1978) refers to the spectral flux terms as "transfers."

form of a cutoff wavenumber filter (LaCasce 1996). The small-scale dissipation was found to represent only a few percent of the total energy budget. Its influence is included in our diagnosis of the residual term and thus forms part of the uncertainty estimate. The mean flow had upper-layer velocity $\overline{u}_1 = 0.1$ and lower-layer velocity $\overline{u}_2 = 0$. Thus the mean flow projected onto the barotropic mode, but this was observed to have no effect on the eddy statistics or energy budget diagnostics examined here, as might be inferred from $F_{p,0,r} = 0$, $\forall\{p, r, K\}$. The domain $0 \le x \le L_x = 20\pi L_D$, $0 \le y \le L_y = 20\pi L_D$ is discretized with 256^2 grid points, giving a range of resolved wavenumbers $0.1 < k_x, k_y < 12.8$ radians/L_D.

Building on earlier work (e.g., Hua and Haidvogel 1986; Larichev and Held 1995), which noted the sensitivity of QG turbulence to friction, AF focused on this sensitivity. They showed, for instance, that the ratio $\mathrm{KE_{bc}}/\mathrm{KE_{bt}}$ has a maximum value of $\mathrm{KE_{bc}}/\mathrm{KE_{bt}} = 1/\delta$ when bottom friction is strong, and $\mathrm{KE_{bc}}/\mathrm{KE_{bt}} \to 0$ when friction is weak. When friction is moderately strong and stratification is surface intensified, this ratio and other characteristics of model eddies compare well with observations. The strength of friction is measured by the "throughput" parameter, $\mathrm{TP} \equiv (\overline{u}_1 - \overline{u}_2)/R_2 L_D$, where R_2 is the bottom friction decay rate and the numerator is the imposed vertical shear. Table 3 summarizes all runs analyzed here.

4. Results for modal mechanical energy budgets

Here we describe the scale-dependent mechanical energy budget for the runs summarized in Table 3. At a given K, a statistically steady state requires two balances: 1) the sum of all terms must be zero (implying physically there is no net source[5] of energy *for scales smaller than* K),

$$\frac{\partial E^{>}_{p,K}}{\partial t} = \sum_{q,r} (N_{p,q,r} + F_{p,q,r} + D_{p,q,r}) = 0, \qquad (18)$$

and 2) by Eq. (13) the sum of the slopes of all terms must be zero,

$$\frac{\partial E_p(K)}{\partial t} = -\frac{\partial}{\partial K} \sum_{q,r} (N_{p,q,r} + F_{p,q,r} + D_{p,q,r}) = 0 \qquad (19)$$

(implying that physically there is no net source of energy *at that wavenumber* K). We call Eq. (18) the integral budget and Eq. (19) the local budget. Traditionally authors focus on the slopes (Hua and Haidvogel 1986; Larichev and Held 1995). The advantage is that the sources and sinks at each wavenumber are clear. But the direction of the cascades has to be inferred from integrating by eye from K to ∞, generally a difficult task. The advantage of plotting the spectral fluxes is that positive (negative) flux determines unambiguously that the cascade is directed downscale (upscale). We suggest that it is generally easier to estimate a slope by eye than an integral to infinity. LaCasce (1996) makes the further point that spectral fluxes, being related to the transfer by an integral, enjoy the advantage that they are generally smoother, especially for transient experiments. However, for completeness, we have also plotted the corresponding spectral transfers and other spectral density source terms.

a. Default run

Run 1 was identified by AF as comparing most favorably with observations of the vertical structure and horizontal scale of oceanic mesoscale eddies. The ratio of $\mathrm{KE_{bc}}$ to $\mathrm{KE_{bt}}$ was about 1.5, which compares favorably with current-meter records (Wunsch 1997). The stratification is surface intensified ($\delta = 0.2$) and the friction is moderate (TP = 2.5).

1) Baroclinic energy budget

Figure 1a shows the baroclinic integral budget for run 1. The cyan line shows the residual, which results from departure from statistical equilibrium, small-scale dissipation, and round-off error, and thus provides an estimate of the uncertainty. At scales larger than L_D, mean shear forcing (green line) is the dominant source of energy. Scattering from bottom friction (red line) provides a secondary source, consistent with Hua and Haidvogel (1986). The PE flux (purple line) is responsible for cascading the energy further downscale. The PE flux is zero at $K = 0$, implying that this term neither creates nor destroys energy, but merely redistributes it between scales. Its peak amplitude, about 0.225 [units are $(\overline{u}_1 - \overline{u}_2)^3/L_D$], corresponds to the sum of the peaks of the source terms (red and green lines). The results so far are consistent with standard geostrophic turbulence phenomenology, with the possible exception that there is no inertial range carrying this PE to scales smaller than L_D. However, Larichev and Held (1995) also noted a lack of inertial range in their Fig. 4d, plotting $\Pi^{\mathrm{ke}}_{\mathrm{bt},K}$ and $\Pi^{\mathrm{pe}}_{\mathrm{bc},K}$.

Note the large, negative lobe of the black line—the KE flux is upscale, revealing an inverse KE cascade in the baroclinic mode. This is the key contribution to geostrophic turbulence phenomenology revealed in this

[5] By "net source" we mean to include all sinks as well.

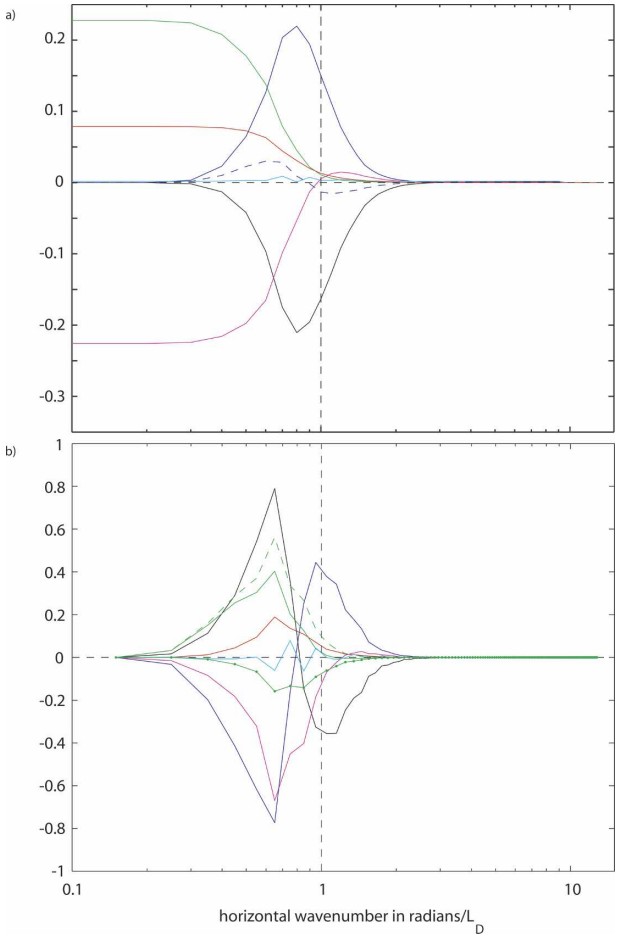

FIG. 1. Baroclinic mechanical energy budget for run 1: moderate friction (TP = 2.5) and surface-intensified stratification ($\delta = 0.2$). (a) Source terms from (18) vs total wavenumber K. (b) Spectral density terms from Eq. (19) (i.e., negative slope of lines in a) vs K. Green is mean shear forcing (with dashed the KE and dotted the PE components), maroon is barotropization, black and purple are fluxes of kinetic and potential energy, respectively, and the dashed purple line is their sum; red is bottom friction dissipation and scattering. The cyan curve is the imbalance due to statistical uncertainty and round-off error. The large negative lobe of the black line in (a) reveals an inverse kinetic energy cascade. Vertical axis in (a) is in units of $(\overline{u}_1 - \overline{u}_2)^3/L_D$, and (b) is in units of $(\overline{u}_1 - \overline{u}_2)^3$. Horizontal axis is in radians per deformation radii.

study. Furthermore, the KE flux is substantial, with peak amplitude almost equal and opposite to the forward PE cascade. Interestingly, this suggests that the baroclinic KE flux might be used to estimate the total forcing of the baroclinic mode via conversion from mean field potential energy to KE. This point will be taken up in section 5. Decomposing the KE flux into its two contributions (see Table 2), we found that the catalytic contribution was stronger than the self-interaction, even though the barotropic mode was less energetic. This suggests that the catalytic term is more efficient at driving the inverse cascade.

Figure 1b plots the corresponding terms in the local budget Eq. (19). At scales smaller than the deformation radius ($K > 1$) the balance is simple: conversion from PE to KE. At larger scales the story is more complicated with all terms playing a nonnegligible role. The mean shear forcing has a positive contribution from PE forcing (dashed green line) and a negative contribution from KE forcing (green line with dots). The PE forcing is the vortex stretching contribution to shear forcing: $\langle \hat{\psi}^*_{\rm bc} ik_x \hat{\psi}_{\rm bt} \rangle \overline{u}_{\rm bc}/L_D$. The KE forcing is $\langle \hat{\psi}^*_{\rm bc} ik_x \hat{q}_{\rm bt} \rangle \overline{u}_{\rm bc}$. There is no inertial range for the KE cascade—as KE is fluxed to larger scale it is quickly removed from the baroclinic mode. The removal process is mostly accomplished by the barotropization (maroon line), which is the dominant nonconservative negative term at large scales in Fig. 1b. Insofar as the surface reflects the baroclinic mode, this is consistent with SW's hypothesis of barotropization as the primary cause of the apparent arrest of the surface layer cascade seen in altimeter data. As discussed in the next section, ultimately energy is removed from the barotropic mode by bottom friction.

2) BAROTROPIC ENERGY

Figure 2 shows the barotropic energy budget for run 1, with the integral budget in Eq. (18) in Fig. 2a and the local budget Eq. (19) in Fig. 2b. Of course there is no PE flux. As expected, there is a net inverse cascade of KE (black line). At small scales the barotropic mode is experiencing a downscale flux (albeit very tiny), consistent with Salmon (1980) but inconsistent with Fu and Flierl (1980) and Rhines (1977). We are currently working on understanding the origins of this contradiction. However, at scales larger than L_D all theories agree with each other and with the qualitative results shown in Fig. 2.

The important result is the tiny amplitude of the barotropic inverse cascade, which is actually much smaller than found in the baroclinic mode (the vertical scales are the same for Figs. 1a and 2a). Apparently moderately strong bottom friction has substantially weakened the barotropic inverse cascade. With such a weak inverse cascade, the main result of Larichev and Held (1995) is not present here. That is, the generation in the *baroclinic* mode is *not* shifted to scales $L \gg L_D$ (green lines peak around $K = 0.65$ rads L_D^{-1} in Fig. 1b); contrast their Fig. 4c, terms IV and V with our green dotted and green dashed lines, respectively. In the barotropic budget, their barotropization term (their Fig. 4b, term II) is much more spread out than our

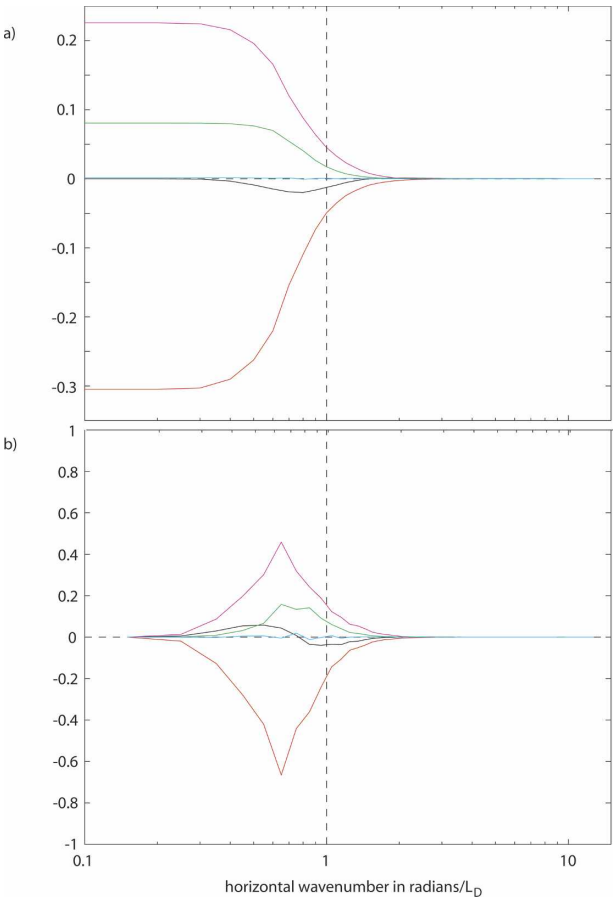

FIG. 2. Same as in Fig. 1, but for barotropic mechanical energy budget.

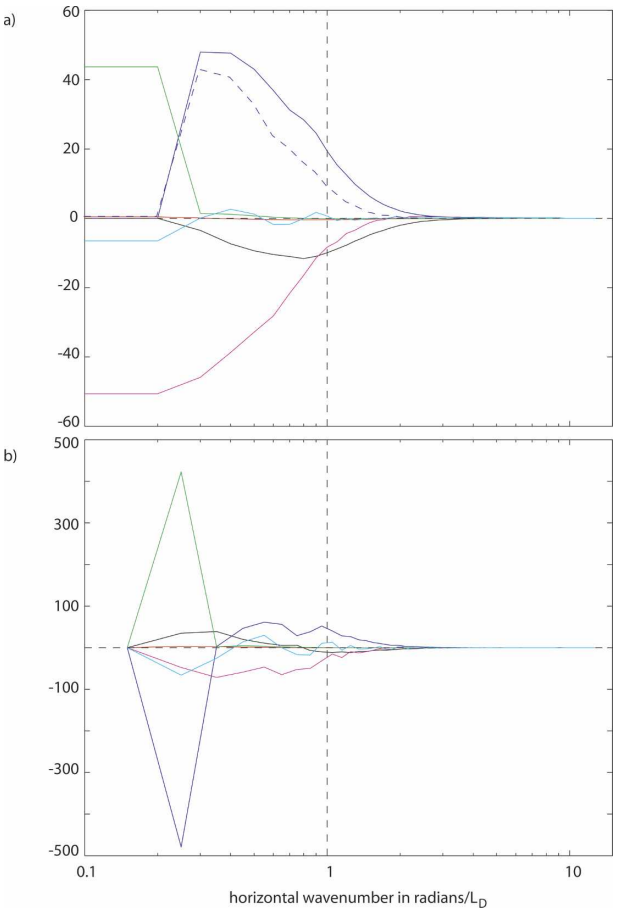

FIG. 3. Same as in Fig. 1, but for run 4, weak friction (TP = 10), and uniform stratification ($\delta = 1$).

strongly peaked barotropization (maroon line in Fig. 2b).

The other terms are unsurprising. Notice that the barotropization term (maroon line) in Fig. 2a is equal and opposite to that in Fig. 1a at $K = 0$, as required. Barotropization is the main source and bottom friction is the sole sink. The inverse cascade is arrested by bottom friction, unlike the case with beta.

b. Robustness of qualitative results

Are the two main results from above sensitive to the two free parameters TP and δ? Here we show that the inverse cascade of baroclinic KE remains strong even for weak friction (larger TP), and uniform stratification ($\delta = 1$). However, not surprisingly, the results of Larichev and Held (1995) are recovered regarding the strong inverse cascade in the barotropic KE, and the resulting shift in baroclinic shear generation to larger scales. Also, barotropization becomes distributed over a wide range of scales for both the baroclinic and barotropic budgets.

Run 4 has weak friction and $\delta = 1$ and is therefore similar to the run analyzed by Larichev and Held (1995). The eddies are much larger and more barotropic than observed oceanic mesoscale eddies. Figure 3 shows the baroclinic energy budget for run 4, with terms from Eq. (18) in Fig. 3a and with terms from Eq. (19) in Fig. 3b. The generation is now extremely concentrated at large-scale $L \gg L_D$ consistent with Larichev and Held (1995). Note that barotropization is actually more spread out. This should be contrasted with the requirement of individual triads, mentioned in section 2b, that the baroclinic–barotropic energy exchange is small except when the barotropic wavenumber is near $K = 1/L_D$. The KE inverse cascade is still present, though its peak amplitude is now only about one-fifth that in the forward PE cascade. However, it is still non-negligible in comparison with the barotropic inverse cascade.

Recall that geostrophic turbulence theory predicts a net forward cascade of total baroclinic energy at large scales (Salmon 1978, 1980). This implies that $\Pi^{\mathrm{ke}}_{\mathrm{bc},K}$ +

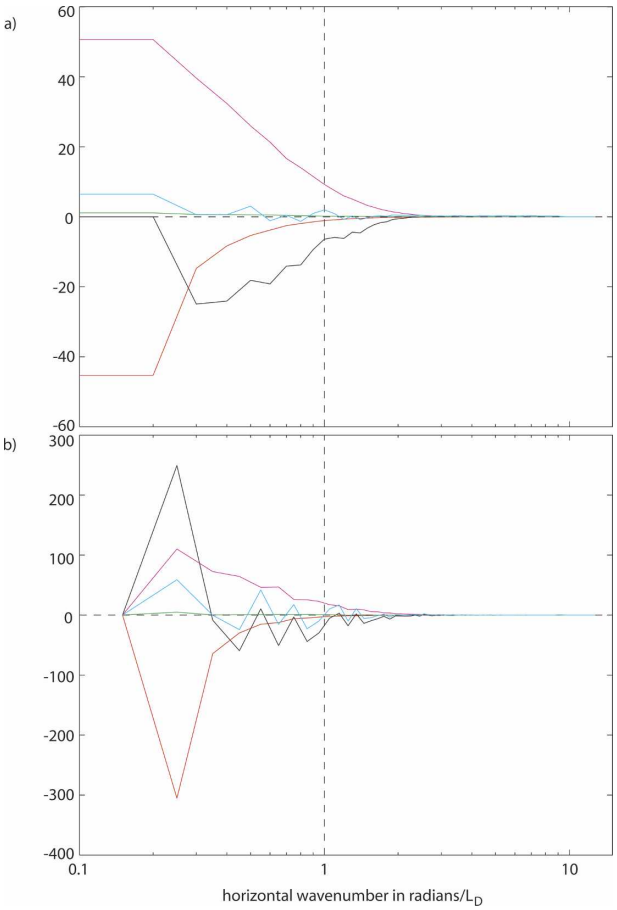

FIG. 4. Same as in Fig. 1, but for the barotropic mode and for run 4, weak friction (TP = 10), and uniform stratification ($\delta = 1$).

$\Pi^{pe}_{bc,K} > 0$. This is certainly true for run 4, which is in a similar parameter regime to Salmon (1980); see dashed purple line in Fig. 3a. For large scales it is also true for run 1; see Fig. la. However, at scales $L \lesssim L_D$ the total energy is cascading upscale in contradiction to the well-known Fig. 1 of Salmon (1980) [reproduced in Fig. 6.6 of Salmon (1998) and Vallis (2006)].

The corresponding barotropic energy budgets are shown in Fig. 4. The barotropic inverse cascade is much stronger than for run 1, but note that the peak baroclinic inverse KE cascade in Fig. 3a is still comparable (about one-half as strong) as the peak barotropic flux. The barotropic forcing is almost exclusively from barotropization (shear forcing is negligible) and is spread over a wide range of length scales, as found by Larichev and Held (1995). Note the clear correspondence between the peaks in bottom friction and inverse cascade in Fig. 4b, suggesting that bottom friction is responsible in arresting the cascade, as Salmon (1978, his Fig. 7b) found.

5. Relating the upper-layer cascade with the baroclinic mode and depth-integrated energy budget

A strong motivation for this work is to help interpret the spectral KE flux estimates made from altimeter data. The classic theory (e.g., Salmon 1980) however is mostly framed in terms of barotropic and baroclinic modes (since the relationship between the streamfunction and potential vorticity is diagonal using that vertical basis set). So SW related the altimeter signal to the baroclinic modes insofar as possible, based on the hypothesis that the altimeter data reflect the first baroclinic mode more than the barotropic mode, as argued by Wunsch (1997) and Smith and Vallis (2001). Here we test the consistency of this hypothesis with our simple model simulations. The upper layer of the model will be taken as our "surface signal," as this offers a more direct comparison with altimeter data (a point emphasized by AF). For this reason we have diagnosed the upper-layer scale-dependent integral mechanical energy budgets, derived in section 2d, and described the phenomenology below. The lower-layer integral budget is also described briefly. Attention is given to exploring the possibility of using the satellite data to infer the depth-integrated forcing.

a. Default run

For run 1 the upper-layer scale-dependent integral mechanical energy budget Eq. (14) is shown in Fig. 5a by dashed lines. All the terms are important. The results look similar to the corresponding baroclinic budgets, so we have selected colors to correspond to the analogous terms in Fig. la and replotted those terms with solid lines and with the bottom friction scattering and shear forcing combined (now green line). Upper-layer forcing $F_{1,K}$ is the dominant source at large-scale (green), upper-layer advection of vortex stretching $\Pi^{pe}_{1,K}$ drives a strong forward cascade (purple), and an equally strong upper-layer inverse KE cascade $\Pi^{ke}_{1,K}$ (black) fluxes the energy to larger scale where it is transferred to the lower layer $C_{1,K}$ (maroon). The latter term was estimated as a residual for computational convenience. Uncertainty estimates are not available for the upper-layer integral budget but will be provided for the depth-integrated integral budget (Fig. 6).

This close agreement suggests that all the upper-layer scale-dependent mechanical energy budget terms have close connection with the baroclinic terms, at least in the run that compares best to oceanic observations. This is the second main contribution of this work. The interpretation of the satellite measurements of SW,

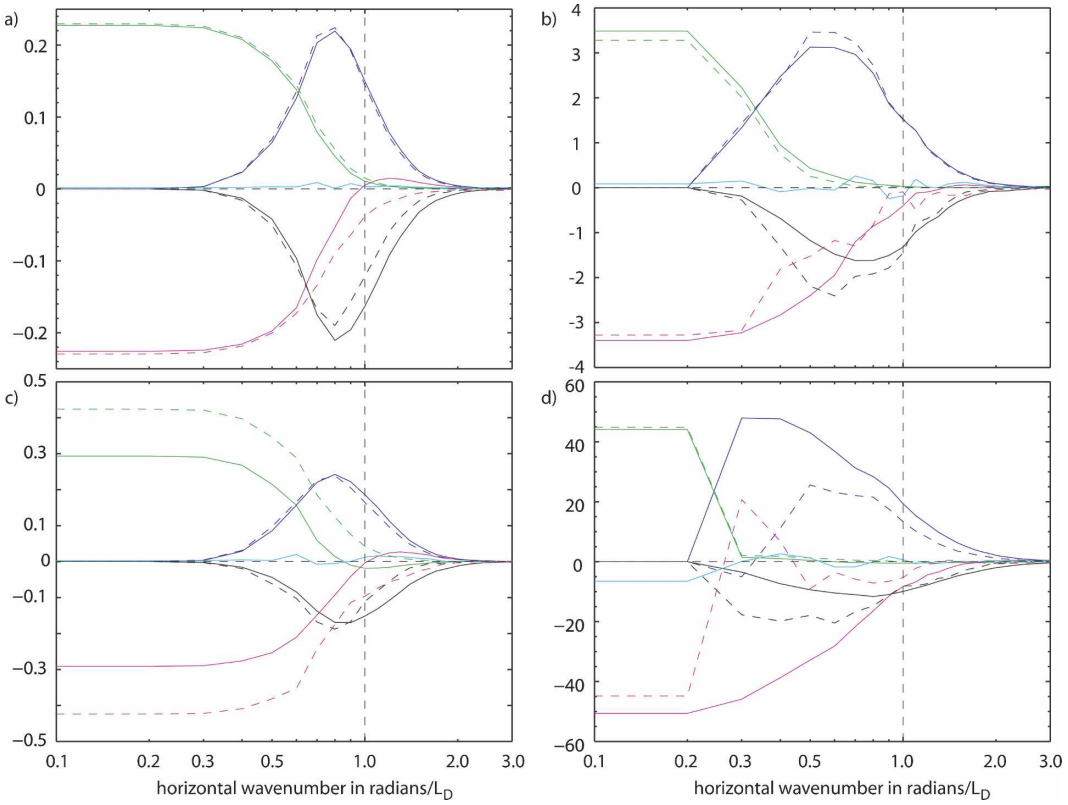

FIG. 5. Comparison of upper-layer and baroclinic mode scale-dependent integral mechanical energy budget: (a) run 1, (b) run 2, (c) run 3, and (d) run 4. Solid lines are baroclinic mode. Colors as in Table 1, but shear forcing and bottom friction have been combined (green line). Dashed lines for upper layer, with colors corresponding to analogous term in baroclinic budget: forcing (green), vortex stretching flux (purple), conversion to lower layer (maroon), and KE flux (black).

$$\Pi^{\mathrm{ke}}_{\mathrm{bc},K} \approx \Pi^{\mathrm{ke}}_{1,K}, \tag{20}$$

is just a special case of this more general principle.

For the default run, the lower-layer budget (not shown) was dominated by upper- to lower-layer conversion and bottom friction dissipation. The forcing was zero, and the lower-layer cascades were tiny in this case and did not correspond well with those in the barotropic mode.

b. *Robustness of the upper-layer baroclinic correspondence*

The argument for the correspondence between upper-layer and baroclinic KE flux [Eq. (20)] relied on surface-intensified stratification and at least as much KE in the baroclinic mode as in the barotropic mode (SW). So our most extreme deviation from this here is run 4, which had $\delta = 1$ and was highly barotropic. Encouragingly, the relationship in Eq. (20) is not too far off even for this run. In Fig. 5d, the upper-layer KE flux follows closely the baroclinic KE flux at scales $L < L_D$. At larger scales the barotropic contribution becomes important, driving a strong inverse cascade that dominates the surface KE flux. The peak amplitude of the upper-layer inverse cascade (≈ -20) is roughly twice that of the baroclinic cascade (≈ -10). The correspondence between the upper-layer and baroclinic integral budget terms works surprisingly well for the forcing, but not at all well for the other terms. For more realistic parameters (especially run 1, but also runs 2 and 3) the correspondence works much better (see remaining subplots of Fig. 5).

c. *Can we infer the mechanical energy budget from the upper-layer KE flux alone?*

As explained in the introduction, we also seek a relation between the observable surface-layer flux and terms of interest in the depth-integrated, scale-dependent mechanical energy budget. We find that for the most oceanic-like run 1 the upper-layer KE flux alone allows for a good estimate of the rate of PE to KE conversion, and a reasonable estimate for total forcing. For the other runs the relationship is not as strong, but surprisingly useful.

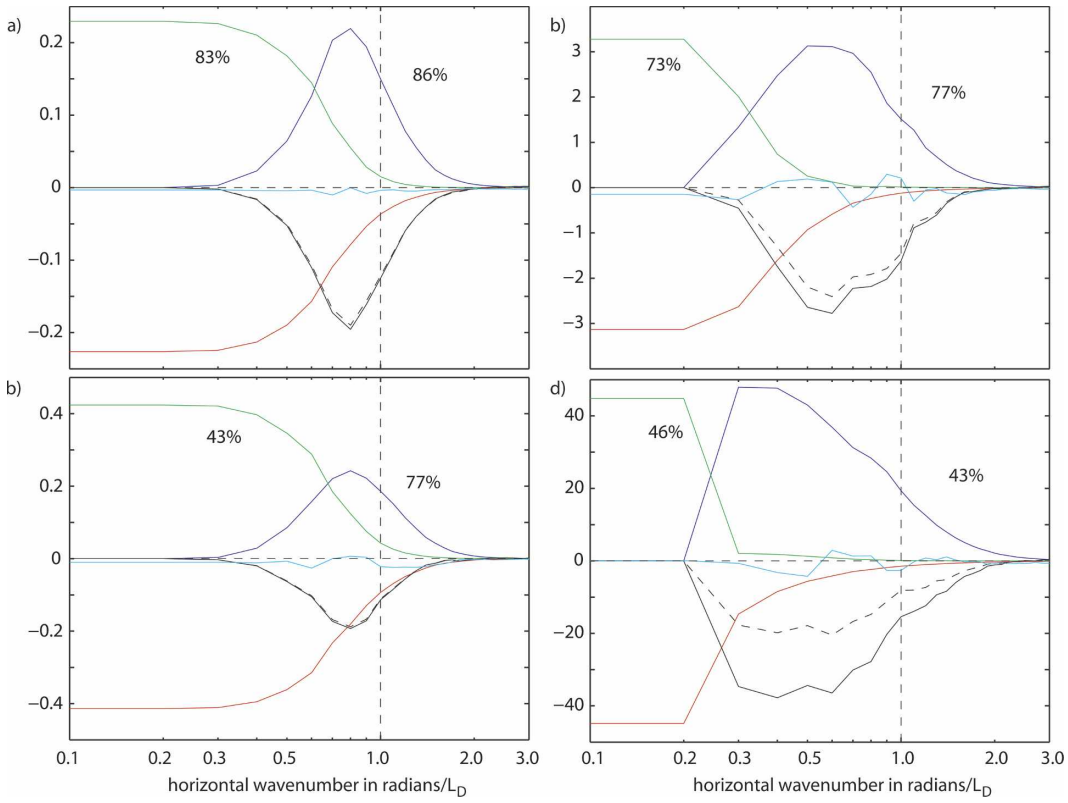

FIG. 6. Comparison of upper-layer kinetic energy flux (dashed lines) and depth-integrated, scale-dependent integral mechanical energy budget (solid lines): (a) run 1, (b) run 2, (c) run 3, and (d) run 4. Colors as in Fig. 5; red denotes bottom friction and cyan denotes residual and represents uncertainty. Percentages are ratios of peak KE flux (left) to peak forcing rate and (right) to peak PE flux.

The depth-integrated, scale-dependent integral energy budget, that is, the sum over the layer budgets [Eq. (14)], is plotted in Fig. 6 for all four runs (solid lines) along with the surface KE flux (dashed). Unlike the barotropization terms, which cancel at $K = 0$ but not necessarily locally (LaCasce 1996), the energy exchange between layers cancels locally. Thus the residuals in Fig. 6 represent the uncertainty (cyan lines) due to statistical nonequilibrium, small-scale dissipation, and numerical errors. In all cases the PE flux (purple) looks much like the reflection about the horizontal axis of the depth-integrated KE flux (solid black). But for runs 1 and 3 the depth-integrated KE flux is barely distinguishable from the upper-layer KE flux (dashed black). This occurs because the moderate friction has damped the lower layer such that its KE is much less than the upper layer (see Table 3) and the KE flux involves velocity to the third power. Even for the high TP runs, the upper-layer KE flux (multiplied by -1) gives a qualitative picture of the PE flux. The worst case is run 4. The ratio of the peak upper-layer KE flux to the peak PE flux is shown as a percentage in the right of each subplot, suggesting that we might infer about 80% of the rate of PE to KE conversion for the ocean from knowledge of the surface KE flux. The total forcing is usually slightly higher than this conversion rate, so its percentage inferred from just the upper-layer KE flux is slightly poorer (see numbers in the left of the subplots).

These results suggest that one can estimate the depth-integrated KE flux, and related quantities of interest, using only surface streamfunction (from satellite altimetry) and knowledge of the mean stratification (from hydrographic climatology). It will be important to confirm this in more realistic models.

d. A quantitative comparison between observed surface KE energy flux, wind forcing, and simulated $\Pi^{\mathrm{ke}}_{I,K}$

The spectral KE flux of the default run peaks at about 0.2 $[(\overline{u}_1 - \overline{u}_2)^3/L_D]$. With a 10 cm/s shear and $L_D = 50$ km, this corresponds to about 4 mW m^{-2} km^{-1}. With $H = 5$ km and $\delta = 0.2$, this gives 4 mW m^{-2} as an estimate of the upper-layer flux (and therefore the depth-integrated flux), close to the global mean rate of wind forcing 2.68 $\pm$ 0.17 mW m^{-2} estimated from

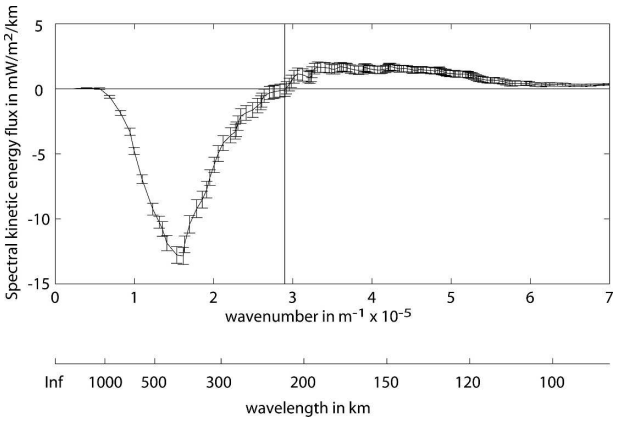

FIG. 7. The spectral kinetic energy flux associated with the near-surface geostrophic flow in the Kuroshio Extension region from altimeter data (approximately 24° to 46°N × 156° to 174°E). The straight vertical line indicates the wavenumber of the first baroclinic deformation scale, taken from Chelton et al. (1998), averaged over the region of the spectral flux estimate, and should be compared with unity in the other figures. Because the vertical structure is not known, the units are per unit depth. This plot is fairly typical of results from other regions of the World Ocean, though the zero crossing is typically more to the left of the deformation scale and the forward flux is typically larger, often about 1/3 of the upscale flux.

National Centers for Environmental Prediction (NCEP) wind stress and satellite altimetry (Scott 1999). In the Kuroshio Extension region the surface spectral flux is several times larger, because of stronger currents in this region, implying a PE to KE conversion rate around 15 mW m^{-2} (Fig. 7). The mean shear probably changes by at least a factor of 10 from the western boundary to midgyre, implying variations in the strength of spectral flux of the order of a thousand times, which is consistent with results from altimeter data.

e. Qualitative difference between observed surface KE energy flux and simulated upper-layer $\Pi^{\mathrm{ke}}_{1,K}$

It is interesting to note a quantitative difference between the spectral flux in the upper layer and that estimated from the satellite altimetry. The peak *forward flux* in the altimeter data generally attains maxima about ⅓ of the peak *upscale flux* throughout most of the South Pacific and about ⅙ in the Kuroshio Extension region (Fig. 7). The model upper-layer flux did experience a forward flux but it was so small that it is barely identifiable in these figures. For example, the maximum upscale upper-layer flux is more than 85 times larger than the maximum upper-layer downscale flux in Fig. 5a.

It appears that some dynamics not contained in the two-layer model may be driving a stronger forward cascade near the surface of the real ocean. Perhaps unbalanced motion, or the higher baroclinic modes, provide a pathway to small-scale dissipation. Resolving this discrepancy may provide important clues to the mechanical energy pathways toward dissipation in the real ocean. The authors are currently pursuing this.

6. Conclusions

Here we summarize our findings with succinct answers to the four questions raised in the introduction.

1) Is the inverse KE cascade seen at the oceanic surface due to the barotropic mode? Our model results suggest that partially it is, though its contribution is very small except for the weak friction runs, and only for scales about 50% larger than L_D. The baroclinic mode makes the most significant contribution; see Fig. 5, especially Fig. 5a, which shows the simulation we regard as the most representative of midlatitude oceanic conditions (weak friction yields eddies that do not compare well with observations; AF).
2) Is it possible that the baroclinic mode experiences an inverse KE cascade? Yes, as speculated by SW, baroclinic KE at scales larger than L_D cascades to larger scale. In fact in the most oceanically representative run the baroclinic inverse KE cascade is almost 10 times the barotropic inverse KE cascade.
3) How are the cascades of the surface and baroclinic modes related? The spectral KE flux in the upper layer times the upper-layer fractional depth provides a very good approximation to the baroclinic spectral fluxes, as expressed in approximation (20), for run 1 (see Fig. 5a). In fact, all the terms in the scale-dependent integral mechanical energy budget have close correspondence with their analogous baroclinic mode terms.
4) Given knowledge of the surface flux, what additional information is needed to infer the depth-integrated spectral flux, and other terms of interest to the mechanical energy budget? Insofar as the two-layer model is appropriate, we would only need to know the fractional depth of the upper layer. This could be inferred from the time mean density stratification, which is available for the World Ocean (Conkright et al. 2002). Although the two-layer model is crude, it still may provide our current best estimate of the conversion rate of gravitational potential energy to KE in the ocean.

We hope that the results described herein are equally interesting to the geostrophic turbulence theorist, and

those interested in quantifying the oceanic mechanical energy cycles from oceanic observations. While the inverse KE cascades are likely robust phenomena, the relationship between the upper layer and the baroclinic mode may be model dependent. It is important to investigate this relationship in more realistic models that include, for instance, multiple layers, bottom topography, and horizontally varying mean flows.

Acknowledgments. The idea for this paper grew from conversations with K. Shafer Smith and Rick Salmon, and their continuing profound influence on RBS's work is gratefully acknowledged. RBS thanks Sergey Danilov for pointing out a misleading statement in the abstract of his earlier work, Scott and Wang (2005). Glenn Flierl provided useful feedback as acknowledged in the text. Gary Mitchum and Bo Qiu provided helpful feedback on interpreting altimeter data. We also appreciate two anonymous reviewers for their useful feedback and patience. The altimeter products have been produced by the CLS Space Oceanography Division as part of the European Union's Environment and Climate project AGORA (ENV4-CT9560113) and DUACS (ENV4-CT96-0357) with financial support from the CEO program (Centre for Earth Observation) and the Midi-Pyrenees regional council. Data were made available by the AVISO/Altimetry operations center. Hydrographic data have been provided by the U.S. National Oceanographic Data Center via the *World Ocean Atlas 2001*. We thank Dudley B. Chelton, Roland A. deSzoeke, and Michael G. Schlax for making the Rossby radius data available (from the Web site http://www.coas.oregonstate.edu/research/po/research/chelton/index.html). A portion of the computing was performed at Texas Advanced Computing Center (TACC), The University of Texas at Austin. RBS was supported by NSF Grants OCE-0327520, OCE-0326515, and OCE-0526412. BKA started this collaboration while at Princeton University, and he acknowledges financial support from NSF Grant OCE-0327189 while at Princeton, and a Jackson School of Geological Sciences Development Grant for support while at UT Austin.

APPENDIX

Useful Identities

a. The Jacobian

It follows from the definition of the Jacobian,

$$\mathbf{J}(a, b) \equiv \frac{\partial a}{\partial x}\frac{\partial b}{\partial y} - \frac{\partial a}{\partial y}\frac{\partial b}{\partial x},$$

that

$$\mathbf{J}(a, b) = -\mathbf{J}(b, a),$$

and in particular $\mathbf{J}(a, a) = 0$.

Using the chain rule one finds that

$$\mathbf{J}(ab, c) = a\mathbf{J}(b, c) + b\mathbf{J}(a, c).$$

On a periodic domain or with homogenous Dirichlet boundary conditions, integration by parts reveals that

$$\langle \mathbf{J}(ab, c) \rangle = 0.$$

So clearly

$$\langle a\mathbf{J}(b, c) \rangle + \langle b\mathbf{J}(a, c) \rangle = 0;$$

see Gkioulakas and Tung (2007).

b. Other properties

From the definitions of the high- and low-pass filters,

$$a_K^> + a_K^< = a.$$

Using the Jacobian properties above,

$$\mathbf{J}(a, a_K^>) = \mathbf{J}(a_K^<, a_K^>).$$

REFERENCES

Arbic, B. K., and G. R. Flierl, 2003: Coherent vortices and kinetic energy ribbons in aymptotic, quasi two-dimensional *f*-plane turbulence. *Phys. Fluids,* **15,** 2177–2189.

——, and ——, 2004: Baroclinically unstable geostrophic turbulence in the limits of strong and weak bottom Ekman friction: Application to midocean eddies. *J. Phys. Oceanogr.,* **34,** 2257–2273.

Charney, J., 1971: Geostrophic turbulence. *J. Atmos. Sci.,* **28,** 1087–1095.

Chelton, D. B., R. A. deSzoeke, M. G. Schlax, K. E. Naggar, and N. Siwertz, 1998: Geographical variability of the first baroclinic Rossby radius of deformation. *J. Phys. Oceanogr.,* **28,** 433–460.

Conkright, M., R. Locarnini, H. Garcia, T. O'Brien, T. Boyer, C. Stephens, and J. Antonov, 2002: World Ocean Atlas 2001: Objective analyses, data statistics, and figures: CD-ROM documentation. National Oceanographic Data Center Internal Rep. 17, Silver Spring, MD, 17 pp.

Danilov, S. D., and D. Gurarie, 2000: Quasi-two-dimensional turbulence. *Phys.-Uspekhi,* **43,** 863–900.

Flierl, G. R., 1978: Models of vertical structure and the calibration of two-layer models. *Dyn. Atmos. Oceans,* **2,** 341–381.

Frisch, U., 1995: *Turbulence, the Legacy of A. N. Kolmogorov*. Cambridge University Press, 296 pp.

Fu, L.-L., and G. R. Flierl, 1980: Nonlinear energy and enstrophy transfers in a realistically stratified ocean. *Dyn. Atmos. Oceans,* **4,** 219–246.

Gkioulakas, E., and K. K. Tung, 2007: A new proof on net upscale energy cascade in 2d and QG turbulence. *J. Fluid Mech.,* in press.

Held, I. M., and V. D. Larichev, 1996: A scaling theory for hori-

zontally homogeneous, baroclinically unstable flow on a beta plane. *J. Atmos. Sci.,* **53,** 946–952.

Hua, B. L., and D. B. Haidvogel, 1986: Numerical simulations of the vertical structure of quasi-geostrophic turbulence. *J. Atmos. Sci.,* **43,** 2923–2936.

Killworth, P. D., D. B. Chelton, and R. A. de Szoeke, 1997: The speed of observed and theoretical long extratropical planetary waves. *J. Phys. Oceanogr.,* **27,** 1946–1966.

Kobashi, F., and H. Kawamura, 2002: Seasonal variation and instability nature of the North Pacific Subtropical Countercurrent and the Hawaiian Lee Countercurrent. *J. Geophys. Res.,* **107,** 3185, doi:10.1029/2001JC001225.

Kraichnan, R. H., and D. Montgomery, 1980: Two-dimensional turbulence. *Rep. Prog. Phys.,* **43,** 547–619.

LaCasce, J. H., 1996: Baroclinic vortices over a sloping bottom. Ph.D. dissertation, Massachusetts Institute of Technology–Woods Hole Oceanographic Institution Joint Program, 220 pp.

Larichev, V. D., and I. M. Held, 1995: Eddy amplitudes and fluxes in a homogeneous model of fully developed baroclinic instability. *J. Phys. Oceanogr.,* **25,** 2285–2297.

Lesieur, M., 1997: *Turbulence in Fluids.* 3d ed. Vol. 40, *Fluid Mechanics and Its Applications,* Kluwer Academic, 515 + xvi pp.

Pedlosky, J., 1987: *Geophysical Fluid Dynamics.* 2d ed. Springer-Verlag, 710 pp.

Rhines, P. B., 1977: The dynamics of unsteady currents. *The Sea,* E. Goldberg et al., Eds., Vol. 6, John Wiley and Sons, 189–318.

Salmon, R., 1978: Two-layer quasi-geostrophic turbulence in a simple special case. *Geophys. Astrophys. Fluid Dyn.,* **10,** 25–52.

——, 1980: Baroclinic instability and geostrophic turbulence. *Geophys. Astrophys. Fluid Dyn.,* **15,** 167–211.

——, 1998: *Lectures on Geophysical Fluid Dynamics.* Oxford University Press, 378 pp.

Scott, R. B., 1999: Geostrophic energetics and the small viscosity behaviour of an idealized ocean circulation model. Ph.D. dissertation, McGill University, 124 pp. [Available from Schulich Library of Science and Engineering, Macdonald Stewart Library Building, McGill University, 809 Sherbrooke St., West Montreal, PQ, Canada H3A 2K6.]

——, and F. Wang, 2005: Direct evidence of an oceanic inverse kinetic energy cascade from satellite altimetry. *J. Phys. Oceanogr.,* **35,** 1650–1666.

Smith, K. S., and G. K. Vallis, 2001: The scales and equilibration of midocean eddies: Freely evolving flow. *J. Phys. Oceanogr.,* **31,** 554–571.

——, and ——, 2002: The scales and equilibration of midocean eddies: Forced–dissipative flow. *J. Phys. Oceanogr.,* **32,** 1699–1720.

Spall, M. A., 2000: Generation of strong mesoscale eddies by weak ocean gyres. *J. Mar. Res.,* **58,** 97–116.

Stewart, R. H., C. Shum, B. Tapley, and L. Ji, 1996: Statistics of geostrophic turbulence in the Southern Ocean from satellite altimetry and numerical models. *Physica D,* **98,** 599–613.

Treguier, A.-M., and B. L. Hua, 1988: Influence of bottom topography on stratified quasi-geostrophic turbulence in the ocean. *Geophys. Astrophys. Fluid Dyn.,* **43,** 265–305.

Vallis, G. K., 2006: *Atmospheric and Oceanic Fluid Dynamics: Fundamentals and Large-Scale Circulation.* Cambridge University Press, 744 pp.

Wunsch, C., 1997: The vertical partition of oceanic horizontal kinetic energy and the spectrum of global variability. *J. Phys. Oceanogr.,* **27,** 1770–1794.

——, and R. Ferrari, 2004: Vertical mixing, energy, and the general circulation of the oceans. *Annu. Rev. Fluid Mech.,* **36,** 281–314.